Available online at www.sciencedirect.com
ScienceDirect
Trans. Nonferrous Met. Soc. China 35(2025) 1585−1602
Transactions of Nonferrous Metals Society of China
www.tnmsc.cn

Creep behavior of powder metallurgy Ni-based superalloys with minor scandium

Li-ming TAN[1,2], Lin YE[1,2], Heng DONG[1,2], Xiao-qiong OUYANG[1,2], Xiang-you XIAO[1,2], Qi ZENG[3], Jing-wei CHEN[3], Lan HUANG[1,2], Feng LIU[1,2]

1. State Key Laboratory of Powder Metallurgy, Central South University, Changsha 410083, China;
2. Research Institute of Powder Metallurgy, Central South University, Changsha 410083, China;
3. AECC Hunan Aviation Powerplant Research Institute, Zhuzhou 412000, China

Received 9 July 2024; accepted 18 November 2024

Abstract: The creep behavior of two PM superalloys, U720Li and RR1000, each alloyed with trace amount of Sc, was systematically investigated. Findings reveal that RR1000 alloy with 0.064 wt.% Sc (R-0.064) demonstrates superior creep resistance compared to U720Li alloy with 0.043 wt.% Sc (U-0.043), at 650 °C and 1000 MPa, and the primary creep mechanisms in both alloys are identified as dislocation shearing and precipitate bypassing. When tested at 700 °C and 700 MPa, the U-0.043 alloy predominantly exhibits micro-twinning and dislocation bypassing, while the R-0.064 alloy engages in extended stacking fault shearing of γ' precipitate, dislocation bypassing and climb. At 750 °C and 460 MPa, dislocation bypassing and climb emerge as the main creep mechanisms for both alloys.
Key words: creep resistance; Ni-based superalloy; scandium; powder metallurgy; γ' precipitate

1 Introduction

Nickel-based polycrystalline superalloys, with excellent comprehensive properties at elevated temperatures, constitute indispensable structural materials for turbine discs [1,2]. In pursuit of enhancing engine efficiency and reducing carbon dioxide and nitrogen oxide emissions, the endeavor to elevate the service temperature and augment the mechanical properties of Ni-based superalloys, encompassing tensile strength, creep resistance, fatigue resistance, and damage tolerance, in extreme operational environments poses a formidable challenge [3−5]. Superalloys with enhanced creep properties allow them to perform reliably under high stress and high temperatures for extended periods, which improves the efficiency, safety, and durability of components used in critical applications. Thereby, within the realm of disc superalloys, considerable attention has been devoted to investigating the creep behavior of polycrystalline alloys at elevated temperatures [6−8].

The strong influence of alloy composition on creep behavior is widely recognized in the field, leading to tremendous works aimed to improve the creep resistance of polycrystalline alloys via composition design. For instance, BAI et al [9] investigated the effect of 0−4.8 wt.% Ta on the creep damage of a polycrystalline Ni-based superalloy ME3, and found that Ta could significantly improve the creep resistance at 650 °C and 980 MPa, while the creep life at 750 °C and 600 MPa of ME3 with Ta exceeding 2.4 wt.% dropped sharply. On the other hand, some other works concerned the synergy and interactions of

Corresponding author: Lan HUANG, Tel: +86-731-88830937, E-mail: lhuang@csu.edu.cn;
Feng LIU, Tel: +86-731-88830940, E-mail: liufeng@csu.edu.cn
https://doi.org/10.1016/S1003-6326(25)66769-0

various elements, more than adjusting one major element on a base alloy. KIM et al [10] developed theoretical models that relate alloy composition with minimum creep rate and creep life, which can be adopted to facilitate composition design. Thereafter, LIU et al [11] recalculated a critical parameter in Kim's model, the multielement diffusion coefficient, via establishing atomic mobility database obtained from high throughput-based experiments. Then, data-driven methods integrating machine learning and refined physical models were adopted to screen compositions with aimed properties from over 6×10^5 candidates, and finally obtained two polycrystalline superalloys with superior creep resistance.

Nonetheless, it is important to note that these models are typically established based on an extensive array of experiments, and their applicability to alternative composition systems awaits further investigation. It has been substantiated that rare earth elements are beneficial to tailoring the microstructure and mechanical properties of superalloys. KANG et al [12] found that yttrium microaddition, precisely 0.05 wt.%, can significantly refine the grain of Inconel 713C by segregating at the grain boundaries and improve the high-temperature properties. Besides Y [13−16], La [17−19] and Ce [20−22] are also found to be beneficial for superalloys. Recently, Sc has been reported to have similar benefits on the superalloy. DENG et al [23] demonstrated that Sc had a good affinity to oxygen which could purify the grain boundary and reinforce tensile properties. YE et al [24] optimized the addition of Sc in two typical powder metallurgy superalloys, U720Li and RR1000, through investigation on the microstructure and tensile properties of these Ni-based superalloys with different Sc contents. It was concluded that U720Li with 0.043 wt.% Sc and RR1000 with 0.064 wt.% Sc had superior mechanical properties at ambient and elevated temperatures, which are attributed to the comprehensive effects of γ' precipitate modification and grain boundary strengthening [24]. However, the creep mechanism of polycrystalline superalloys alloyed with minor Sc is unrevealed.

In this study, a systematic investigation was conducted to analyze the creep behaviors of two PM superalloys, i.e., U720Li and RR1000, both of which were alloyed with a minor addition of Sc, offering valuable insights for potential performance enhancement in turbine discs.

2 Experimental

The compositions of two typical powder metallurgy (PM) superalloys, U720Li and RR1000, two typical and broadly applied PM superalloys for turbine engines, enhanced with minor Sc additions of 0.043 wt.% Sc and 0.064 wt.% Sc and designated as U-0.043 and R-0.064, respectively, are presented in Table 1. These superalloys were synthesized through a series of processes including vacuum induction melting (VIM), gas atomization, hot extrusion, and heat treatment. The production commenced with the creation of master alloys via VIM. Subsequently, powders with a particle size below 150 μm were produced through argon atomization and sieving. These powders were then consolidated through hot extrusion at 1130 °C, employing an area reduction ratio of 16:1. The final step involved heat treatment of the billets, which differed for each alloy. Specifically, U-0.043 billets underwent heat treatment at 1095 °C for 4 h, followed by oil quenching, and then aged at 760 °C for 16 h with air cooling. In contrast, R-0.064 billets were solution-treated at 1120 °C for 4 h, followed by air quenching, and subsequently aged at 760 °C for 16 h, also followed by air cooling. Thereafter, the creep tests were conducted at 650, 700, and 750 °C, with initial stresses of 1000, 700, and 460 MPa, respectively.

Electron backscatter diffraction (EBSD) was employed to examine the initial microstructure and internal deformation post-creep deformation. Prior to EBSD analysis, the samples were sectioned and polished using abrasive papers and 50 nm colloidal silica, followed by vibrational polishing to alleviate

Table 1 Chemical compositions of two PM superalloys containing Sc (wt.%)

Superalloy	Cr	Co	Mo	W	Al	Ti	Zr	C	B	Hf	Sc	Ni
U-0.043	15.9	14.3	3.23	1.5	1.8	4.34	0.021	0.025	0.012	−	0.043	Bal.
R-0.064	14.4	19.5	4.97	1.84	2.6	3.19	−	0.03	0.02	0.45	0.064	Bal.

surface stress induced by mechanical processing. Post-EBSD examination was evaluated using HKL Channel5 software. Additionally, the geometrically necessary dislocation (GND) densities were determined using the open-source MTEX program. Furthermore, the microstructural characteristics and fracture morphologies were investigated using a Quanta 650 FEG field-emission scanning electron microscope (FE-SEM) equipped with an EBSD detector. To elucidate the interactions between γ' phase and dislocations, the transmission electron microscopy (TEM) analysis was conducted using an FEI Tecnai F30 field-emission TEM at an accelerating voltage of 200 kV.

3 Results

3.1 Initial microstructure

As illustrated in Fig. 1, the grains within the heat-treated superalloys exhibit a uniform and refined structure. Notably, the average grain sizes (AGSs) of the U-0.043 and R-0.064 alloys were measured to be 8.99 and 6.09 μm, respectively.

The γ' morphologies and size distributions within the U-0.043 and R-0.064 alloys are detailed in Fig. 2, revealing a trimodal distribution of γ' particles in both alloys. Typically, the larger and more irregularly shaped primary γ' particles are predominantly situated along the grain boundaries. The secondary γ' particles, which constitute a larger fraction of the microstructure, assume cubic shapes in U-0.043 and spherical shapes in R-0.064. Notably, the U-0.043 alloy exhibits secondary γ' particles with an average size of 390.1 nm and a volume fraction of 23.9%. In contrast, the R-0.064 alloy features a greater number and finer secondary γ' particles, with an average size of 143.1 nm and a volume fraction of 28.8%. In both alloys, the diminutive, spherical γ' particles, approximately 30 nm in size, are interspersed among the larger secondary γ' particles.

3.2 Creep behavior

Figures 3 and 4 depict the creep strain−time curves and the variation of creep rate over time for the two alloys, respectively. Under the conditions

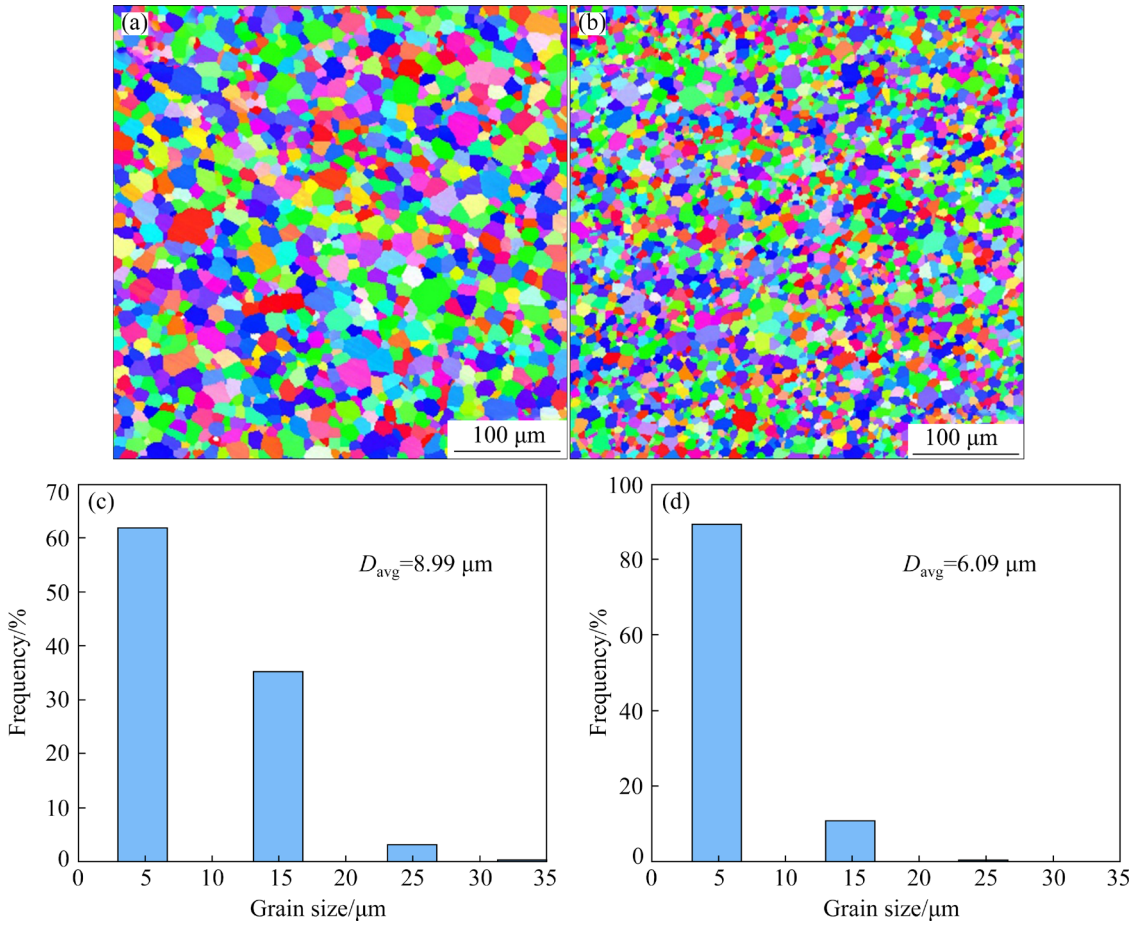

Fig. 1 EBSD IPF images (a, b) and grain size distributions (c, d) of U-0.043 (a, c) and R-0.064 (b, d)

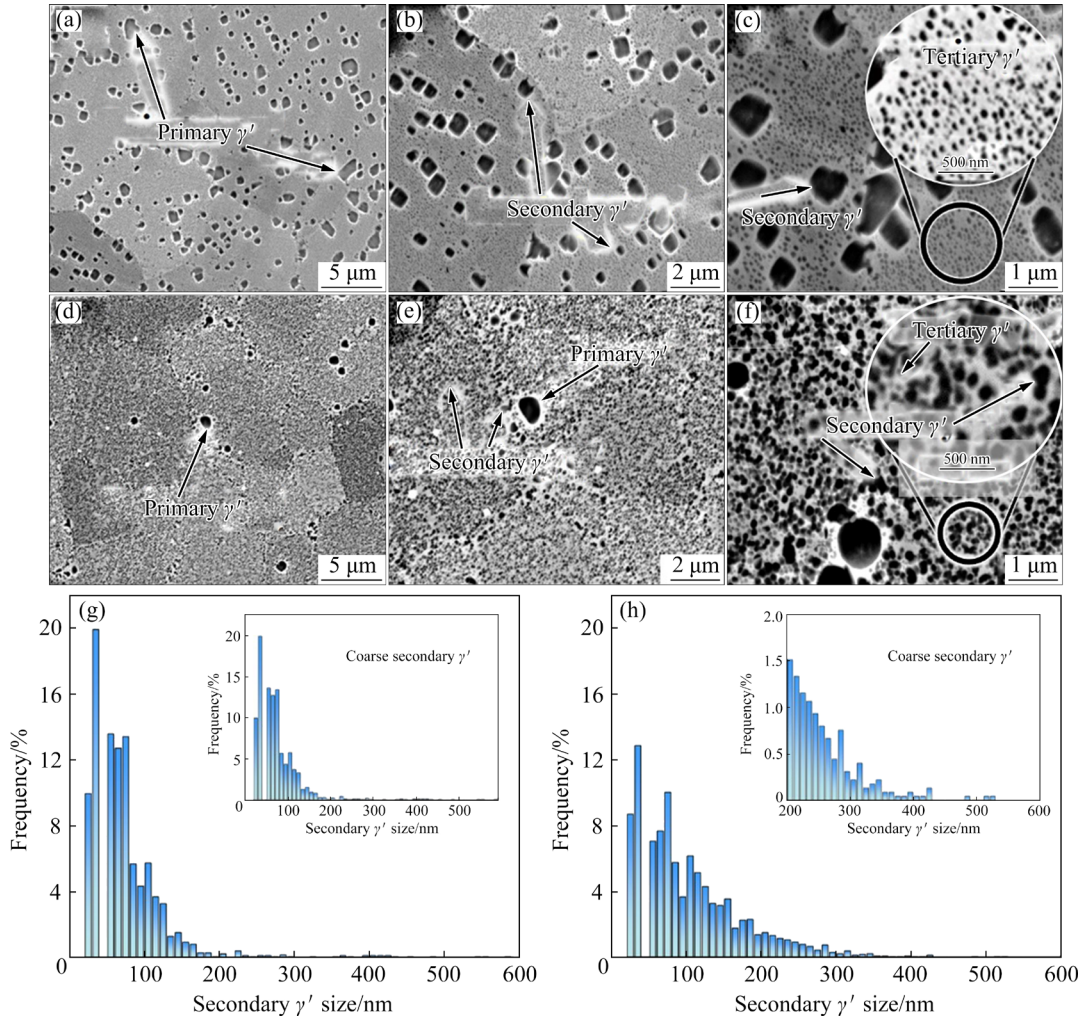

Fig. 2 SEM images showing γ' morphologies of U-0.043 (a−c) and R-0.064 (d−f), with size distributions of secondary γ' in U-0.043 (g) and R-0.064 (h)

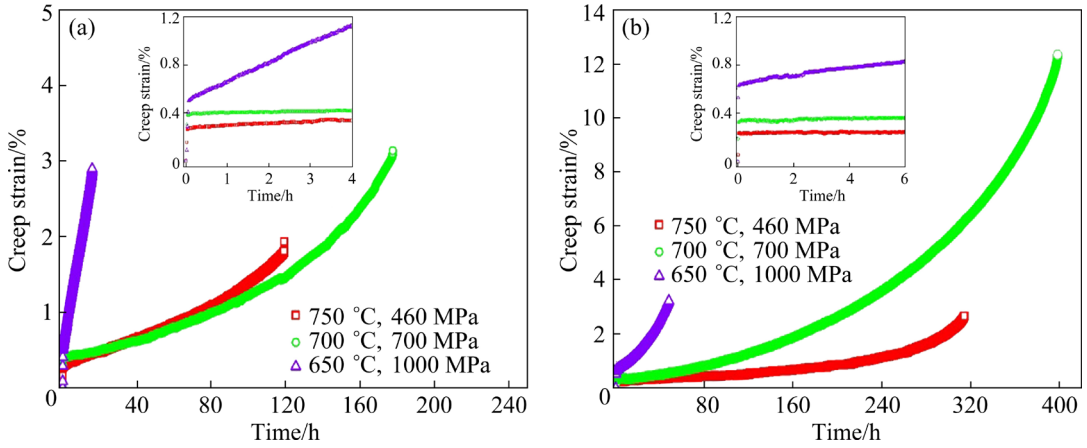

Fig. 3 Strain−time curves of two PM superalloys under different creep conditions: (a) U-0.043; (b) R-0.064

of 700 °C, 700 MPa and 750 °C, 460 MPa, both alloys initially exhibit an increase in strain, which stabilizes at a relatively constant level before surging, dramatically leading to final failure. This behavior demonstrates the complete creep lifecycle for both U-0.043 and R-0.064 alloys, encapsulating the primary, secondary, and tertiary creep stages. Under more rigorous conditions of 650 °C,

1000 MPa, the secondary creep phase is less pronounced, particularly for U-0.043 alloy.

Comparatively, R-0.064 shows significantly better creep resistance than U-0.043 under these testing conditions, as detailed in Table 2. Notably, the creep lifespan of R-0.064 exceeds that of U-0.043 by more than 100% across all tested conditions. Especially, at 700 °C and 700 MPa, R-0.064 shows a creep life of 398.4 h, more than twice that of U-0.043, which achieves 177.5 h. Additionally, minimum creep rate during the steady-state phase of R-0.064 is consistently lower than that of U-0.043. In terms of creep fracture elongation, R-0.064 also demonstrates better performance at 700 °C and 700 MPa, with an elongation of 12.3%, far exceeding that of U-0.043 (3.1%). At 650 °C, 1000 MPa and 750 °C, 460 MPa, R-0.064 still slightly surpasses U-0.043 in elongation. Given that the secondary creep rate is a critical determinant of the overall creep rupture life, lower secondary creep rate and higher creep fracture elongation of R-0.064 contribute to its extended lifespan under these conditions. A comprehensive analysis of the creep behavior, integrating microstructural observations and creep modeling, will be elaborated on subsequent sections.

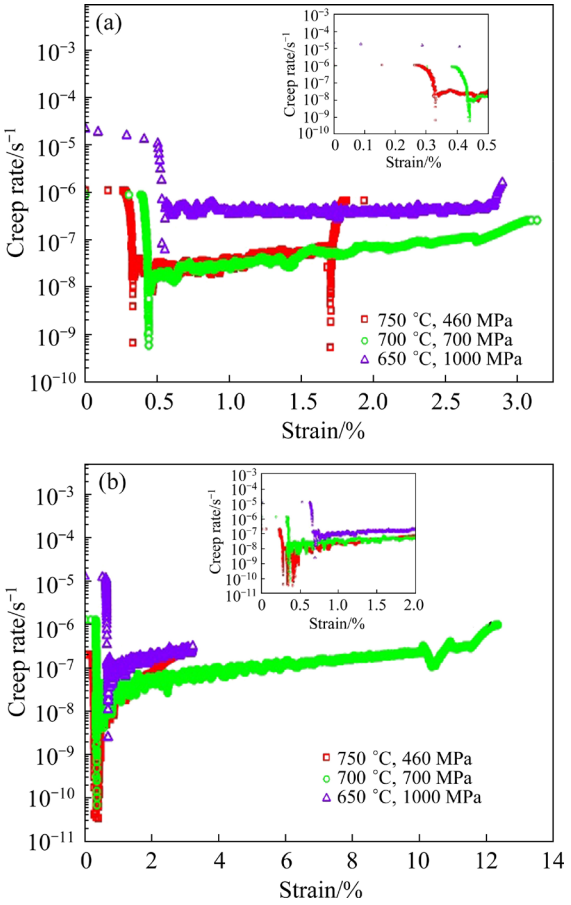

Fig. 4 Creep rate−strain curves of two PM superalloys under different conditions: (a) U-0.043; (b) R-0.064

Table 2 Creep behaviors of U-0.043 and R-0.064 PM superalloys under different conditions

Superalloy	Creep condition	Creep life/h	Creep fracture elongation/%	Minimum creep rate/s^{-1}
U-0.043	650 °C, 1000 MPa	15.8	2.9	4.1×10^{-7}
	700 °C, 700 MPa	177.5	3.1	2.6×10^{-8}
	750 °C, 460 MPa	119	1.9	3.4×10^{-8}
R-0.064	650 °C, 1000 MPa	47.9	3.2	1.5×10^{-7}
	700 °C, 700 MPa	398.4	12.3	3.7×10^{-8}
	750 °C, 460 MPa	314.2	2.7	1.3×10^{-8}

3.3 Microstructure after creep rupture

Figures 5(a_1−c_1) display the macroscopic fracture morphologies of the U-0.043 alloy after creep rupture tests at 650 °C and 1000 MPa, 700 °C and 700 MPa, and 750 °C and 460 MPa. Based on the characteristics of the fracture surfaces, they are divided into three regions: crack initiation, crack propagation, and final fracture areas, marked as ①, ②, and ③, respectively, in Fig. 5. Cracks typically originate at or near the surface of the specimens. In the crack initiation areas of all specimens, intergranular cracking is the dominant feature, as illustrated in Figs. 5(a_2−c_2). Grain boundary strengthening, resulting from grain refinement, plays a positive role in the low-temperature mechanical properties. However, at high temperatures during creep, grain boundaries become susceptible to damage initiation, as grain boundary and intragranular strengths decrease with increasing temperature, while the grain boundary strength decreases more rapidly. As the creep test temperature increases from 650 to 750 °C, intergranular cracks become more pronounced on the fracture surfaces of the specimens. In the crack propagation stage, quasi-cleavage facets are the main features in the fractures under low-temperature and high-stress conditions, i.e., 650 °C and 1000 MPa, indicating

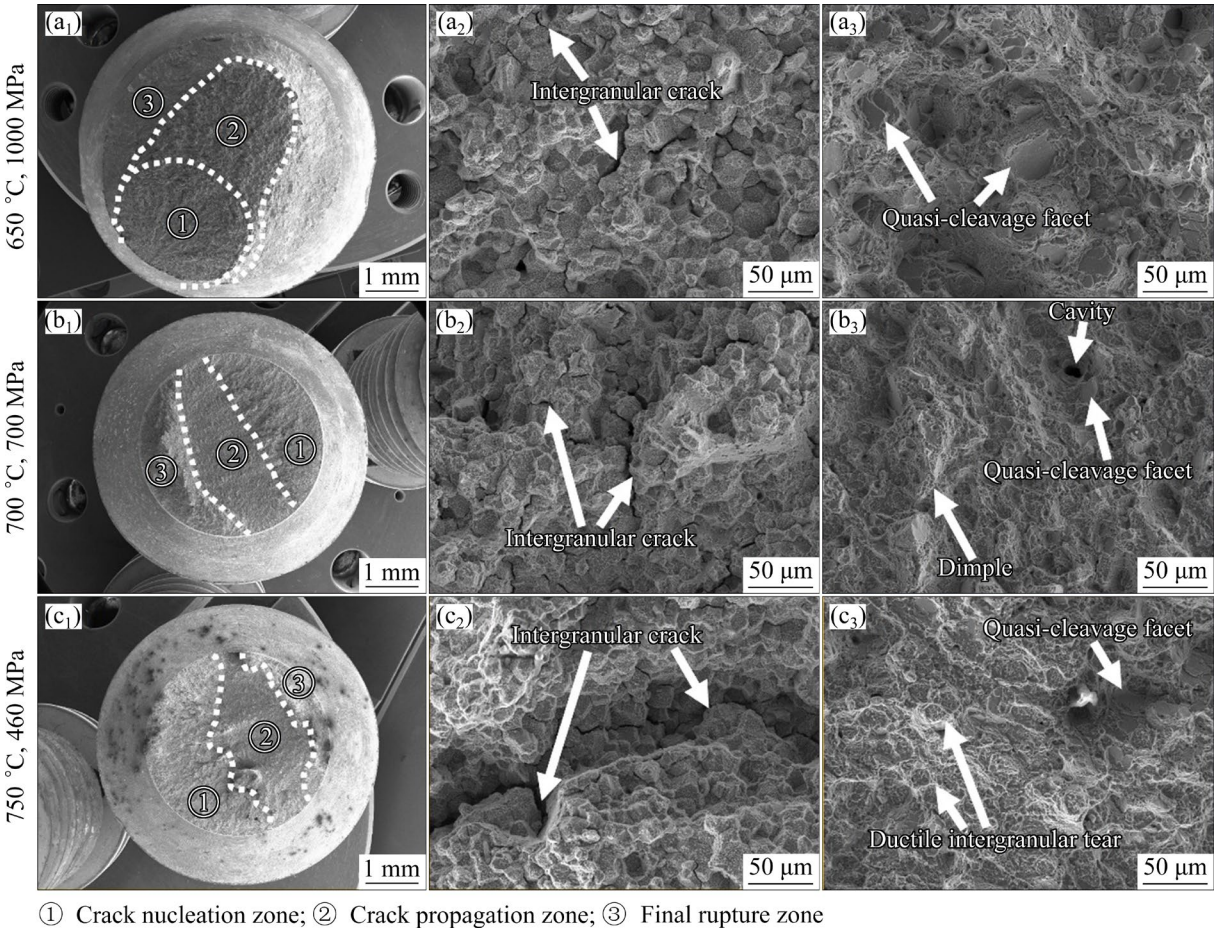

Fig. 5 SEM images showing fracture morphologies of U-0.043 specimens creep-ruptured at 650 °C and 1000 MPa (a_1−a_3), 700 °C and 700 MPa (b_1−b_3), and 750 °C and 460 MPa (c_1−c_3) with magnified images of crack nucleation (a_2−c_2) and propagation (a_3−c_3) zones, respectively

limited plasticity of the specimens under these creep test conditions. With increasing creep test temperature and decreasing applied stress, dimples and tear ridges appear prominently in the crack propagation area, indicating better plasticity of the specimens during the creep process.

Figures 6(a_1−c_1) present the macroscopic fracture morphologies of R-0.064 alloy after creep tests at 650 °C and 1000 MPa, 700 °C and 700 MPa, and 750 °C and 460 MPa. The fracture surfaces of the three samples distinctly exhibit regions of crack initiation, crack propagation, and final fracture. The crack initiation regions in the fractures of the three samples, as illustrated in Figs. 6(a_2−c_2), predominantly feature intergranular cracking. Compared to the fracture surfaces of U-0.043 alloy samples, the intergranular cracking features are more pronounced in the R-0.064 alloy samples, especially in Fig. 6(a_2) where the grain contours within the alloy are clearly visible. Due to the finer grains and increased number of grain boundaries in the R-0.064 alloy, it is more susceptible to crack initiation under high temperature conditions.

Similarly, after the creep test at 650 °C and 1000 MPa, the crack propagation regions in the sample fractures primarily exhibit quasi-cleavage planes, a characteristic similar to the U-0.043 alloy samples under the same testing conditions, indicating quasi-brittle fracture features in both alloys under low temperature and high stress conditions. As shown in Fig. 6(b_3), with the creep test temperature increasing to 700 °C and the applied stress reduced to 700 MPa, some creep voids and dimples appear in the crack propagation regions of the samples; quasi-cleavage planes and dimples, along with some cracks, are found in the final fracture regions, suggesting that the fracture mechanism under these creep test conditions may involve a combination of transgranular and intergranular fracture. When the creep test temperature

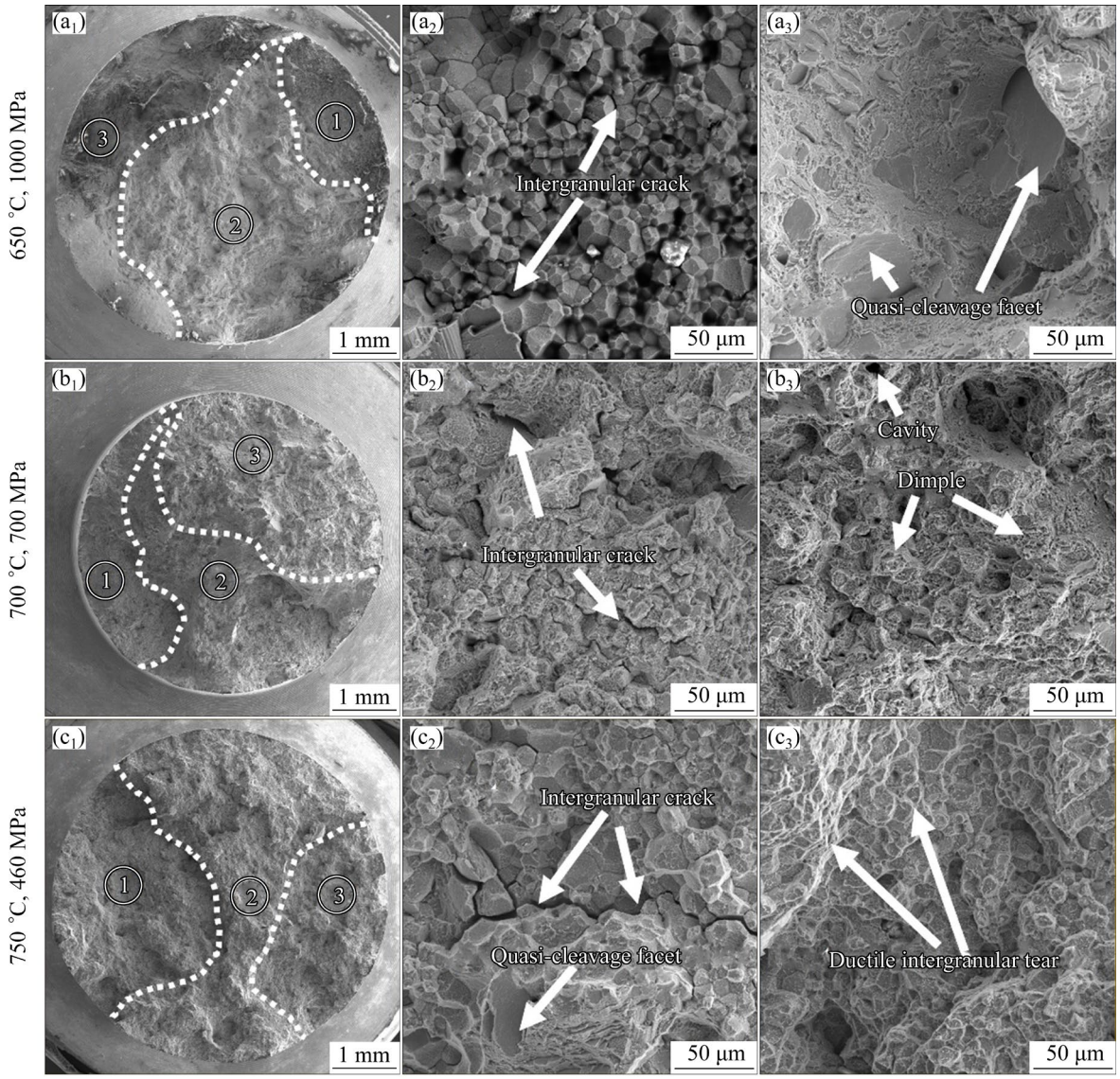

Fig. 6 SEM images showing fracture morphologies of R-0.064 specimens creep-ruptured at 650 °C and 1000 MPa (a_1−a_3), 700 °C and 700 MPa (b_1−b_3), and 750 °C and 460 MPa (c_1−c_3) with magnified images of crack nucleation (a_2−c_2) and propagation (a_3−c_3) zones, respectively

reaches 750 °C with the applied stress reduced to 460 MPa, the crack propagation regions in the sample fractures are dominated by ductile tear ridges, and some ductile tear ridges along with quasi-cleavage planes are still observed in the final fracture regions, displaying characteristics of quasi-brittle fracture.

To investigate the evolution of grain structure and dislocation movement within the alloys after creep testing, the electron backscatter diffraction (EBSD) analysis was conducted on the fracture cross-sections of the creep specimens. The fracture cross-section of the U-0.043 alloy specimen was first analyzed using EBSD, and the results were quantitatively processed to calculate the density of geometrically necessary dislocations (GNDs) using the ATEX open-source software. The grain structure and GND distribution on the fracture cross-section of the specimen after undergoing creep testing at 650 °C and 1000 MPa are shown in Figs. 7(a_1, a_2). Different colors in the figure represent varying densities of GNDs, where transitioning from grey to deep red indicates an increase in the GND density per unit area. A pronounced red area near the fracture of the specimen indicates a high concentration of dislocations, with GND densities

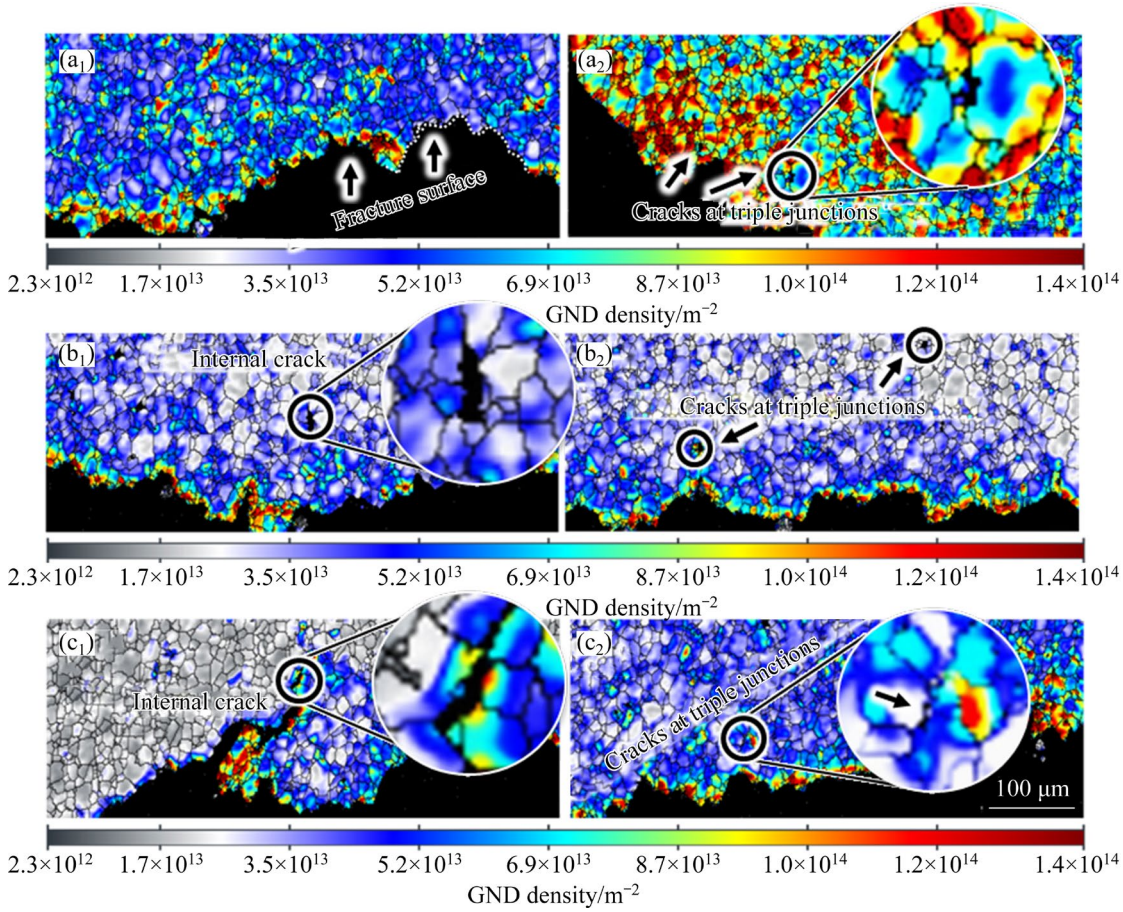

Fig. 7 GND distributions and local misorientations on cross-section of fractured U-0.043 specimens after creep tests at 650 °C and 1000 MPa (a_1, a_2), 700 °C and 700 MPa (b_1, b_2), and 750 °C and 460 MPa (c_1, c_2)

exceeding 10^{14} m^{-2}. GNDs are primarily concentrated at grain boundaries, especially near the fracture zone, where dislocation density is higher, as clearly depicted in Fig. 7(a_2). Farther from the fracture, the color transitions to deep blue, signifying a decrease in dislocation density, with an average GND density in the specimen around 5.28×10^{13} m^{-2}.

The grain structure and GND distribution on the fracture cross-section of the specimen after creep testing at 700 °C and 700 MPa are illustrated in Figs. 7(b_1, b_2). Deep red colors are observed only at the edges of the fracture, mainly concentrated at the grain boundaries, indicating higher dislocation densities at the edges of the fracture. There is also a notable presence of high dislocation densities at the intersections of triple grain boundaries where some have initiated cracks, and significant local misorientation is observed at internal crack locations, indicating substantial strain concentration around them. Moreover, the transition from red at the edge of the fracture to deep blue and finally to grey-white towards the interior of the specimen indicates a gradual decrease in dislocation density. The average GND density in this specimen is about 3.24×10^{13} m^{-2}, which is significantly lower than that in the specimen tested at 650 °C and 1000 MPa. This suggests that lower temperatures and higher stresses facilitate the activation of dislocation bypass and cutting mechanisms, becoming the predominant creep deformation mechanism in the alloy, which will be further detailed in the subsequent transmission electron microscopy (TEM) characterization.

Figures 7(c_1, c_2) present the grain structure and GND distribution on the fracture cross-section of the specimen after creep testing at 750 °C and 460 MPa. There is a significant accumulation of dislocations around the grain boundaries near the crack tips, with new cracks also initiating. The highest GND densities are primarily located at the grain boundaries near the fracture edge, and high local misorientations are observed in some triple grain boundary areas within this region, providing conditions for crack initiation, as shown in

Fig. 7(c_2). The average GND densities in Figs. 7(c_1) and (c_2) are about 2.33×10^{13} and 3.82×10^{13} m^{-2}, respectively, both lower than those in the specimen tested at 650 °C and 1000 MPa.

These results indicate that the highest GNDs and local misorientations are concentrated at the grain boundaries near the fracture edges, while high dislocation densities are also present in internal areas such as the intersections of triple grain boundaries, providing conditions for the initiation of new cracks and voids.

The GND distributions and local orientation differences for the R-0.064 specimens creep-ruptured at 650 °C and 1000 MPa are shown in Fig. 8. According to Figs. 8(a_1, a_2), the highest GND density is located at the fracture edge. Inside the fracture, a higher dislocation density is primarily distributed at the grain boundaries, while the dislocation density inside the grains is much lower. Cracks initiate at the triple junctions of grain boundaries where dislocation pile-up is severe. The average GND density for this specimen is around 4.65×10^{13} m^{-2}, which is lower than that of the U-0.043 specimens under the same testing conditions.

Figures 8(b_1, b_2) reveal significant dislocation pile-up in the creep specimens at 700 °C and 700 MPa, with the highest dislocation density still located at the grain boundaries near the fracture. There is also a higher dislocation density inside the grains, but the lowest density is found within larger grains. Many triple junctions near the fracture experience severe stress concentration, leading to the initiation of numerous wedge cracks. Some of these cracks, located at short distances from each other, have already linked up to form larger internal cracks, particularly evident in Fig. 8(b_2). The average GND density for this specimen is around 9.10×10^{13} m^{-2}, representing the highest dislocation density.

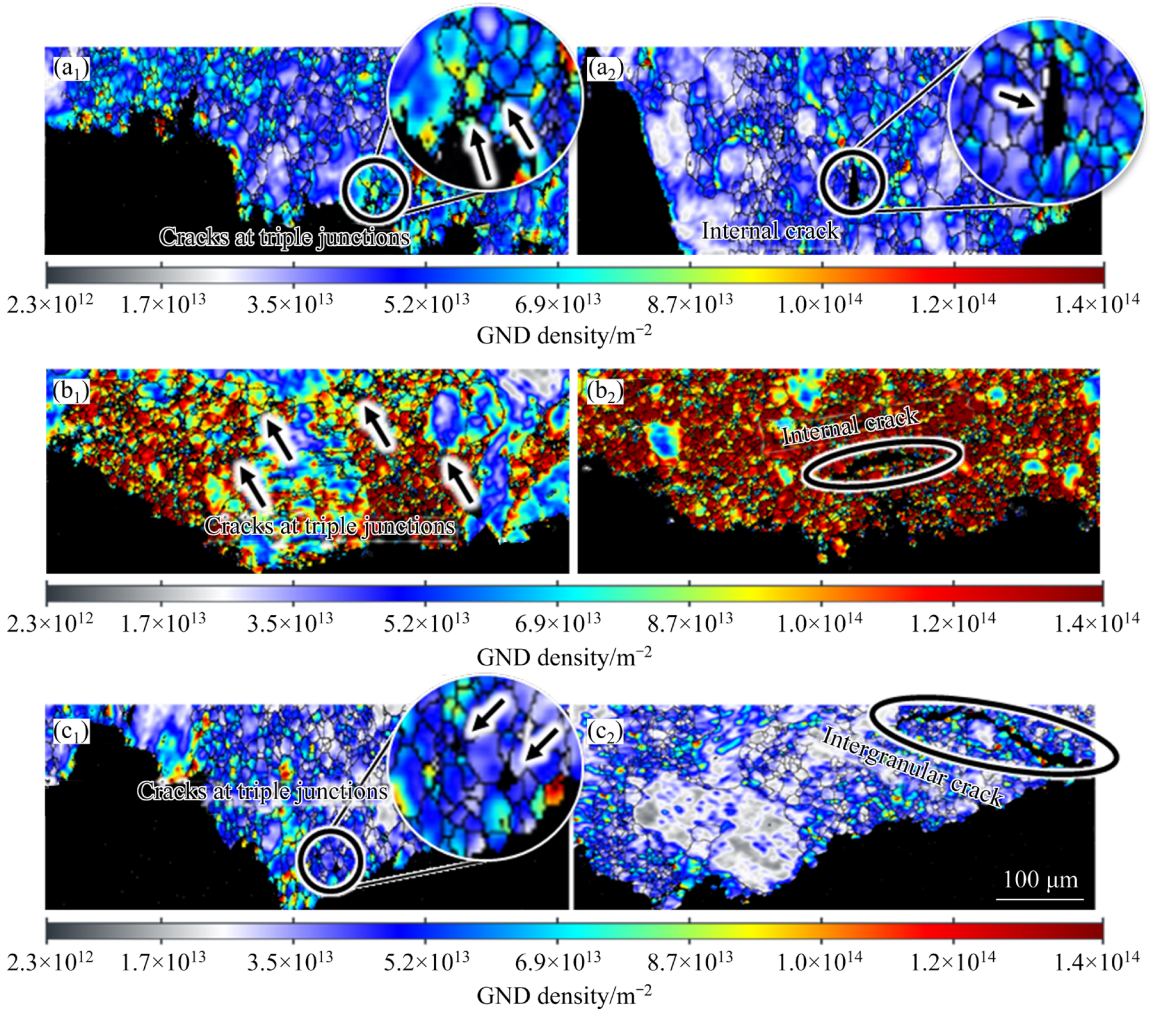

Fig. 8 GND distributions and local misorientations on cross-section of fractured R-0.064 specimens after creep tests at 650 °C and 1000 MPa (a_1, a_2), 700 °C and 700 MPa (b_1, b_2), and 750 °C and 460 MPa (c_1, c_2)

The results from Figs. 8(c_1, c_2) indicate a general reduction in the overall dislocation density for the creep specimens at 750 °C and 460 MPa compared to that at 700 °C and 700 MPa. The highest dislocation densities are still located in similar areas, namely at the grain boundaries near the fracture and inside the fracture. The dislocation density within larger grains significantly decreases. The average GND density for this specimen is about 4.20×10^{13} m^{-2}, which is higher than that of the U-0.043 specimens under the same conditions. This suggests that dislocation motion plays a more significant role in enhancing the creep life of R-0.064 alloy specimens; moreover, this creep condition may not cause severe dislocation pile-up compared to the specimens at 700 °C and 700 MPa. Additionally, certain triple junctions become focal points for crack initiation, with intergranular cracks propagating inside the specimen, consistent with previously discussed fracture morphologies.

A summary of the average GND densities near and inside the cracks of U-0.043 and R-0.064 alloys under three creep conditions is presented in Table 3. Firstly, all six creep specimens demonstrate a common pattern where the highest GNDs are predominantly distributed at the fracture edges of the grain boundaries. Moreover, dislocation motion is particularly impeded at the triple junctions inside the fracture, leading to significant dislocation pile-up and severe stress and strain concentration, thereby providing favorable conditions for crack initiation and propagation. Secondly, in the lower temperature and higher stress creep condition of 650 °C and 1000 MPa, fracture surfaces of both alloys display higher GND density. Furthermore, for the U-0.043 alloy, when the creep temperature increases and the applied stress decreases, the creep life is extended, and the GND density decreases, indicating possible presence of other deformation mechanisms, such as micro-twinning. A similar trend of GND density reduction is observed in the R-0.064 specimens at 750 °C and 460 MPa, whereas in the R-0.064 specimens at 700 °C and 700 MPa, the GND density significantly increases, possibly due to complex interactions between dislocations and precipitates, necessitating more sophisticated techniques to characterize the dislocation configurations in the creep specimens.

Table 3 Average GND densities near and inside cracks of specimens

Superalloy	Creep condition	Average GND density near crack/m^{-2}	Average GND density inside crack/m^{-2}
U-0.043	650 °C, 1000 MPa	5.28×10^{13}	6.61×10^{13}
	700 °C, 700 MPa	3.24×10^{13}	4.16×10^{13}
	750 °C, 460 MPa	3.82×10^{13}	5.80×10^{13}
R-0.064	650 °C, 1000 MPa	4.65×10^{13}	5.68×10^{13}
	700 °C, 700 MPa	9.10×10^{13}	1.08×10^{14}
	750 °C, 460 MPa	4.20×10^{13}	5.65×10^{13}

Figure 9 presents the dislocation configurations within the U-0.043 specimen under 700 °C and 700 MPa creep testing conditions. It is evident that a large number of dislocations are generated during the creep process, and these dislocations interact with the precipitates within the specimen. In Figs. 9(a) and (b), different interactions between dislocations and γ' phases of varying sizes are observed. The secondary γ' phases sized 100−200 nm are sheared by dislocations, leaving behind numerous stacking faults (SFs), as indicated by the blue arrows in the images. In contrast, larger secondary γ' phases (over 300 nm) are more resistant to dislocation shearing, acting as obstacles in the path of dislocation movement. A dense dislocation network is formed as a result of the accumulation of immobile dislocations in front of these larger γ' phases. Figures 9(c) and (d) also show different orientations of stacking faults left behind after shearing of the γ' phases. Additionally, other larger-sized precipitates like carbides within the alloy effectively impede dislocation movement, leading to a certain degree of dislocation entanglement and accumulation around them. Furthermore, the presence of deformation micro-twins (MTs) is also observed in Fig. 9, as indicated by the yellow arrows.

The TEM bright-field image in Fig. 10(a) shows the presence of numerous black stripes in the specimen, with the selected area electron diffraction (SAED) pattern, which indicates that these black stripes are micro-twins. Subsequently, high-resolution transmission electron microscopy (HRTEM) analysis was performed, as shown in Fig. 10(b). The HRTEM results further confirm the presence of a large number of micro-twins in the alloy, with a thickness of about several tens of atomic layers, and these micro-twins are induced by Shockley partial dislocations passing through continuous (111) planes.

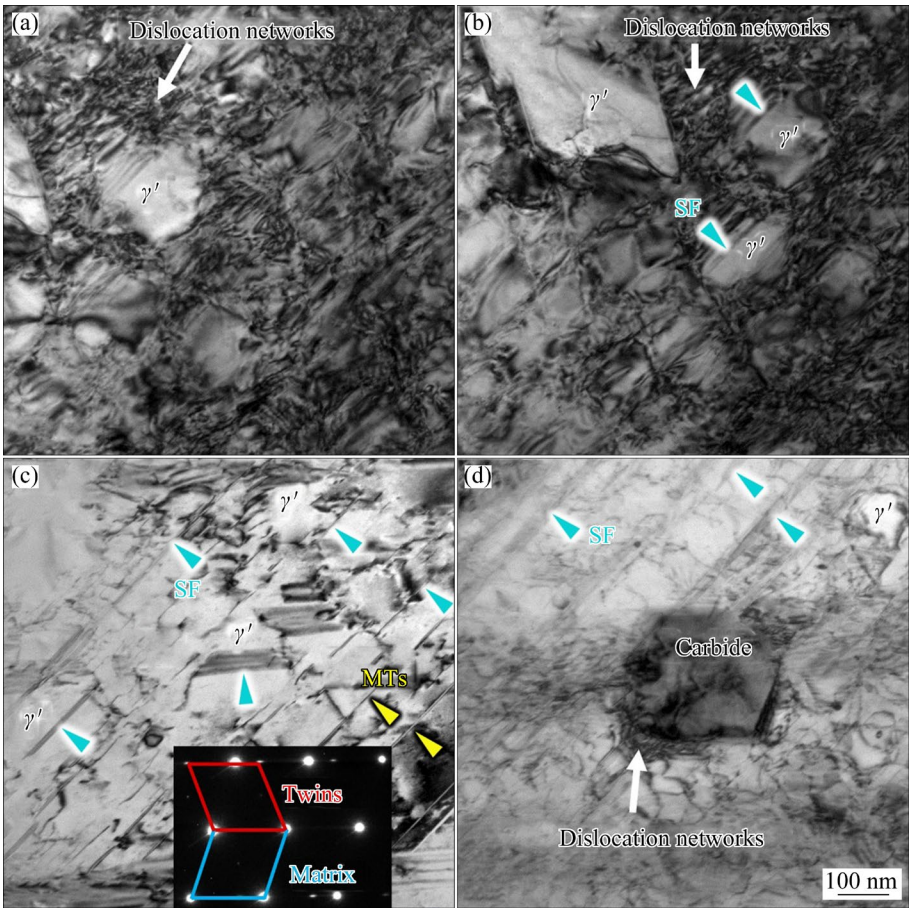

Fig. 9 TEM images showing dislocations in U7-0.043 specimen after creep test at 700 °C and 700 MPa: (a, b) Dislocation networks around γ'; (c) Stacking faults and micro-twins; (d) Dislocation networks around carbide

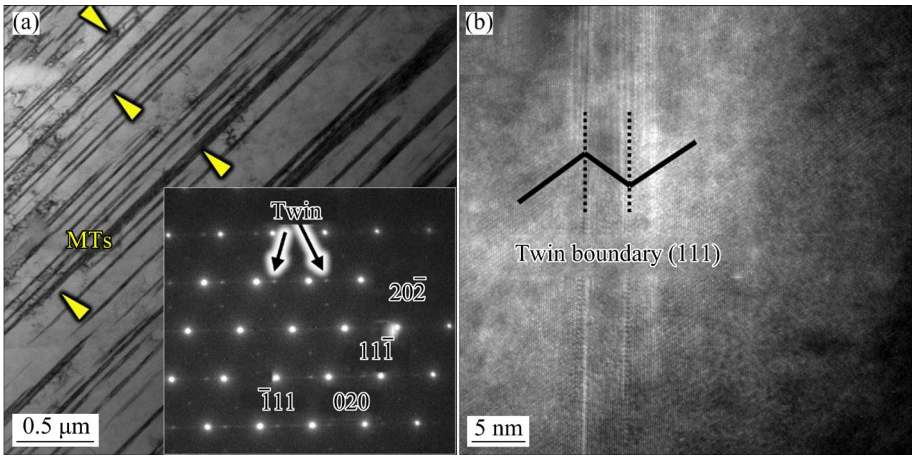

Fig. 10 TEM image with SAED pattern (a) and HRTEM image (b) of micro-twins in U-0.043 specimen after creep test at 700 °C and 700 MPa

Based on the aforementioned results, it is inferred that deformation micro-twinning, stacking fault shearing of precipitates, and partial dislocation bypassing around precipitates are likely deformation mechanisms in the U-0.043 alloy under the creep conditions of 700 °C and 700 MPa. Among these, micro-twinning can effectively impede dislocation movement, thus strengthening the alloy. Dislocations in the alloy can traverse through the twin boundaries and continue moving, thus avoiding dislocation pile-up. Additionally, when cracks in the alloy propagate to the twin boundaries, the difference in crystal orientation on either side of these boundaries causes the cracks to change their

propagation direction. This increases the work done by plastic deformation in the alloy, thereby enhancing its plasticity.

The dislocation configurations in the U-0.043 specimen under the creep test condition of 750 °C and 460 MPa are shown in Fig. 11. It is clearly visible that superlattice intrinsic stacking faults are left by partial dislocations cutting through larger γ' phases, while around these γ' phases, a certain amount of dislocation pile-up occurs due to the impeded dislocation movement. Similarly, Fig. 11(b) shows evident isolated stacking faults in larger secondary γ' phases. Isolated stacking faults caused by $a/2\langle 110\rangle$ dislocations cutting through the γ matrix and the superlattice extrinsic stacking faults are the primary deformation mechanisms when γ' phases are large. The specific origin of isolated stacking faults might be as follows: when $a/2\langle 110\rangle$ perfect dislocations glide to the γ/γ' interface, the increase in creep strain accompanies dislocation accumulation, and when the applied external stress is sufficiently high, it promotes the decomposition of perfect dislocations into $a/3\langle 112\rangle$ partials [25], which then continue to shear the γ' phase and leave behind superlattice extrinsic stacking faults [26]. Figure 11(c) displays a notable dislocation network around larger γ' phases. Moreover, in Fig. 11(d), a unique dislocation configuration is observed, namely unpaired dislocations appearing above or below the γ' phases, indicating a potential thermally-activated dislocation climb mechanism. Similar signs are also evident in Figs. 11(a) and (b), as indicated by the red dotted circles. Under these temperature and stress conditions, extensive dislocation cutting and bypassing might not be fully activated, causing some dislocations to start climbing. Therefore, it is inferred that under the creep test condition of 750 °C and 460 MPa, the main creep mechanisms of the U-0.043 alloy consist of isolated stacking faults produced by dislocation shearing of precipitates, partial dislocation bypassing of precipitates, and dislocation climbing.

After the creep test at 700 °C and 700 MPa, the R-0.064 specimens exhibit a distinctly different dislocation configuration, as shown in Fig. 12. In Figs. 12(a) and (c), it can be seen that larger γ'

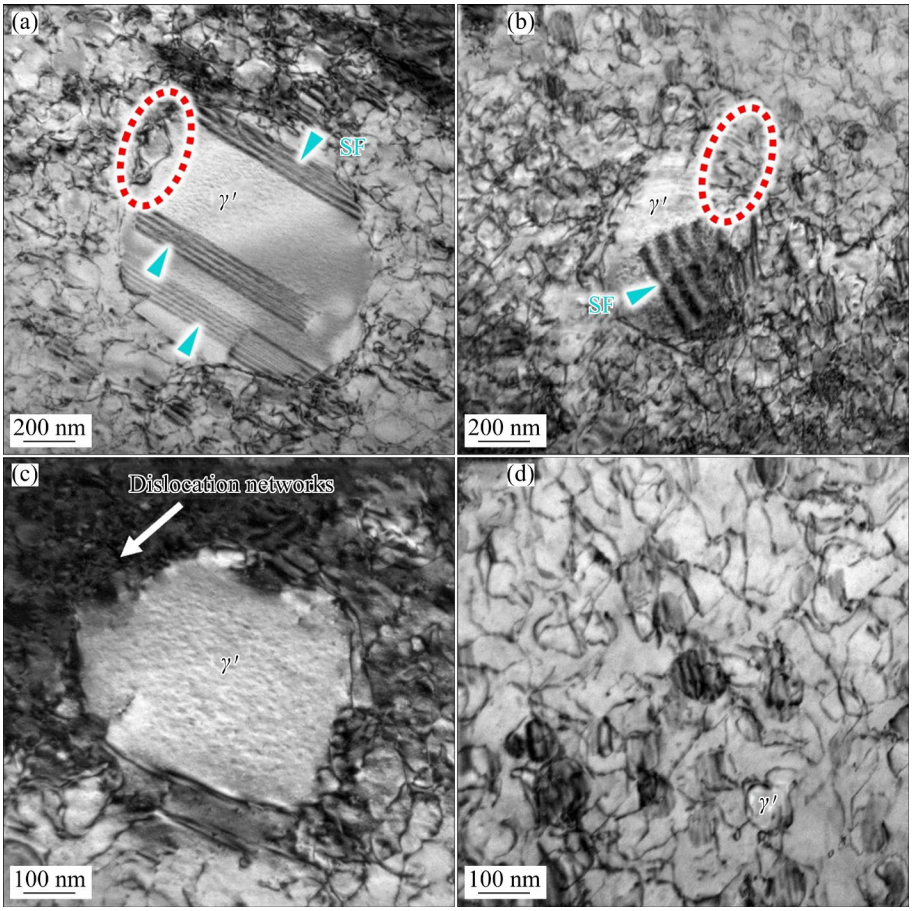

Fig. 11 TEM images showing dislocations in U-0.043 specimen after creep test at 750 °C and 460 MPa: (a, b) Stacking faults in γ'; (c) Dislocation networks around γ'; (d) Dislocation climbing

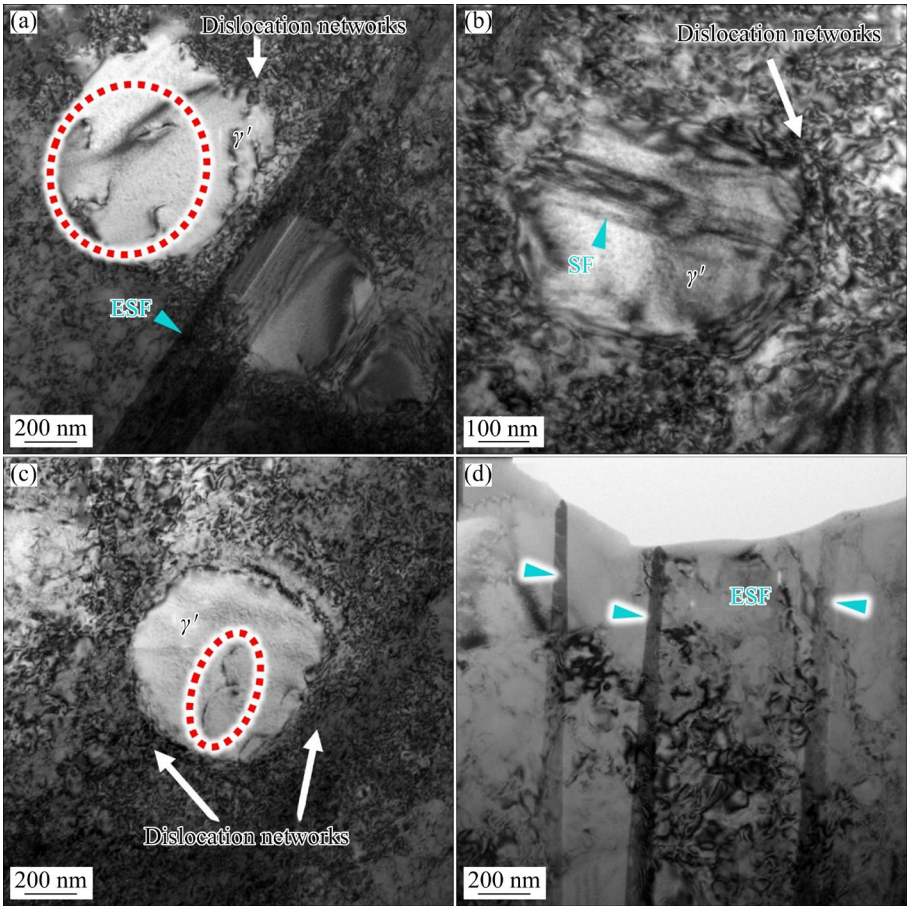

Fig. 12 TEM images showing dislocations in R-0.064 specimen after creep test at 700 °C and 700 MPa: (a, b) Stacking faults in γ' and dislocation networks around γ'; (c) Dislocation networks around γ'; (d) Extended stacking faults

phases could not be sheared by dislocations, resulting in the formation of high-density dislocation networks around them. This is due to larger γ' phases effectively pinning the dislocations and impeding their movement. Additionally, the alloy treated by heat contains small and densely distributed secondary γ' phases, which also make the movement of dislocations more difficult. Therefore, dislocations are more likely to pile up and form prominent dislocation networks in this specimen, consistent with the previously discussed highest GND results. When the size of the γ' phases decreases, some dislocations shear through them, creating stacking faults, while others pile up around them, as shown in Fig. 12(b). Moreover, extended stacking faults (ESFs) are observed in Figs. 12(a) and (d). The formation mechanism of ESFs is similar to that of isolated stacking faults, occurring when a full dislocation of $a/2\langle 110\rangle$ in the γ matrix decomposes, leaving behind an ESF. ESFs represent a transient state during creep deformation, as they have the potential to transform into micro-twins with increasing creep strain [27], although no micro- twins are found in this specimen. Furthermore, in the areas marked by red dashed lines in Figs. 12(a) and (c), some curved dislocation lines are observed on the surface of the larger γ' phases. Their morphology is similar to the dislocations at the γ/γ' interface, suggesting that they might have slipped from the dislocation network and overcome the impediment of the γ' phases through thermally activated climb [5]. Based on these results, the possible deformation mechanisms of the R-0.064 alloy under the creep condition of 700 °C and 700 MPa include extended stacking faults caused by dislocation shearing of precipitates, dislocation bypassing around precipitates, and a minor portion of dislocation climb.

When the creep temperature is raised to 750 °C and the applied stress is reduced to 460 MPa, a large number of unpaired dislocations are observed above or below the γ' phase in the R-0.064 samples, as shown in Figs. 13(a) and (b).

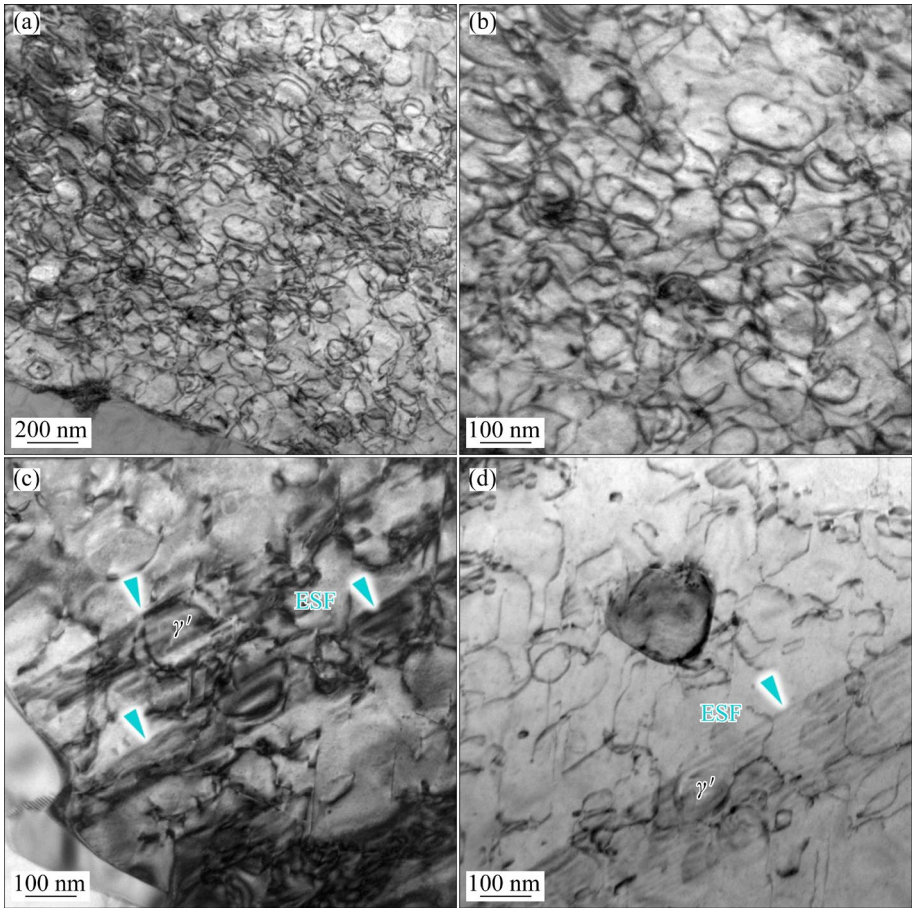

Fig. 13 TEM images showing dislocations in R-0.064 specimen after creep test at 750 °C and 460 MPa: (a, b) Dislocation climbing at different magnitudes; (c, d) extended stacking faults

This is similar to the results reported in the literature [28], and is likely due to thermally activated climb of dislocations. It also resembles the scenario observed in U-0.043 samples under the same creep testing conditions, where the dislocation climbing is even more pronounced. Additionally, the samples exhibit extended stacking faults generated by dislocation shearing, as illustrated in Figs. 13(c) and (d).

4 Discussion

To further investigate the most probable deformation mechanisms under various creep conditions, theoretical calculations were conducted on the critical stresses (CSs) required for various deformation mechanisms in the two alloys under different creep tests. The potential creep mechanisms primarily include shearing of γ' phases by stacking fault, shearing of γ' phases by anti-phase boundary (APB) coupled dislocation pairs, dislocation bypassing, and dislocation climbing, which can be calculated using the following formulas [5]:

$$\sigma_{SF}=3\sqrt{3}\left[\frac{\pi G(2-v)b}{12(1-v)2d}+\frac{2\gamma_{SF}}{3b}\right] \quad (1)$$

$$\sigma_{APB}=3.06\frac{Gbwf^{1/2}}{\pi d}\left(\frac{\pi d\gamma_{APB}}{wGb^2}-1\right)^{1/2}\left(1+\frac{Cf^{1/2}}{2}\right) \quad (2)$$

$$\sigma_{OB}=\frac{Gb}{2\pi\lambda}\ln\left(\frac{\lambda}{r_0}\right) \quad (3)$$

$$\sigma_{CL}=f^{1.5}\sigma_{OB}/2^{1.25} \quad (4)$$

where σ_{SF}, σ_{APB}, σ_{OB} and σ_{CL} represent the critical stresses required for the aforementioned four deformation mechanisms, respectively; G denotes the shear modulus, v represents Poisson's ratio, b is the amplitude of Burgers vector, d indicates the average size of the γ' phase, γ_{SF} is the stacking fault energy in the matrix containing γ' phase, w signifies the elastic repulsion constant of dislocations in the γ' phase, f is the volume fraction of the γ' phase, γ_{APB} represents the antiphase boundary energy of the γ'

phase, C is a material-related constant, λ indicates the width of the matrix channels, and r_0 is the radius of the dislocation source (comparable to b). In this study, the following material parameters were used: w=2.8 [29], C=1 [29], v=0.35 [30], b=0.254 nm [31], and γ_{SF}=22−33 mJ/m^2 [32−34]. The calculation of γ_{APB} and G followed previous works [5,35]. The width of the matrix channels λ can be expressed by the following equation:

$$\lambda = d(f_P^{-1/3} - 1) \quad (5)$$

where f_P is the volume fraction of γ' phase.

The critical stresses required for different creep mechanisms in the two PM superalloys under various creep conditions can be calculated using the above-mentioned expression, with results shown in Fig. 14. It is evident that the critical stresses required for each creep mechanism strongly depend on the test temperature. The highest critical stress is needed for APB-coupled dislocation shearing of the γ' phase, followed by stacking fault shearing of the γ' phase, while the initiation stress required for dislocation bypassing is relatively low. Dislocation climbing only occurs at relatively high temperatures and requires the lowest critical stress. Moreover, the creep condition of 650 °C and 1000 MPa satisfies the initiation stresses for all creep mechanisms, indicating that under this condition, the dominant creep mechanisms for both alloys are dislocation shearing and bypassing of precipitates, consistent with previous results.

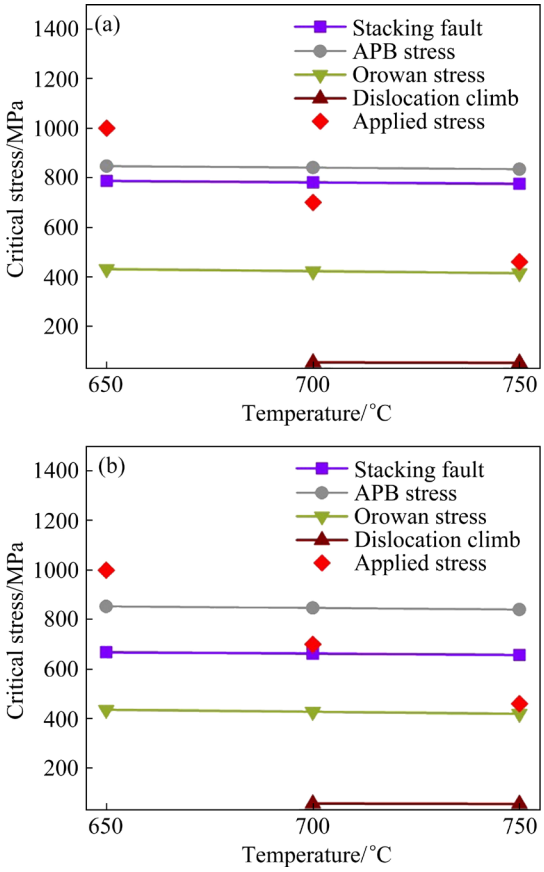

Fig. 14 Critical stresses for different creep mechanisms of two alloys under different creep test conditions: (a) U-0.043; (b) R-0.064

As shown in Fig. 14(a), in the U-0.043 specimen, when the creep temperature is raised to 700 °C, the externally applied stress theoretically is insufficient to initiate stacking fault shearing of the γ' phase, while it meets the initiation stresses for dislocation bypassing and climbing. Combined with the dislocation configuration results from the previous section, it is observed that some smaller γ' phases are sheared by stacking faults under this creep condition. However, a comprehensive analysis suggests that micro-twinning and dislocation bypassing are the primary deformation mechanisms under this creep condition. In contrast, the creep condition of 700 °C and 700 MPa is sufficient to initiate stacking fault shearing of precipitates in the R-0.064 alloy. Along with the dislocation configuration of this specimen, it is inferred that extended stacking faults, dislocation bypassing, and dislocation climbing are its main creep mechanisms. Under the creep condition of 750 °C and 460 MPa, both alloys can initiate dislocation bypassing and climbing, consistent with their respective dislocation configuration results, hence the main creep mechanisms under this condition are dislocation bypassing and dislocation climbing.

5 Conclusions

(1) The U-0.043 and R-0.064 alloys exhibited relatively short lifespans during the creep tests at 650 °C and 1000 MPa. However, their lifespans were extended in the creep tests at 700 °C and 700 MPa, and 750 °C and 460 MPa, with both showing the highest creep lifetimes at 700 °C and 700 MPa, reaching 177.5 and 398.4 h, respectively.

(2) The morphology of the creep fracture surface of the alloys reveals that intergranular cracking is the primary feature in the crack initiation zone. Further examination of the fracture cross-sections indicates that, as the creep

temperature increases and the applied stress decreases, wedge cracks tend to form at the triple junctions of grain boundaries. The geometrically necessary dislocation density and local orientation differences on the fracture cross-sections confirm substantial dislocation pile-up at the triple junctions inside the fracture, leading to severe stress and strain concentration and providing the foundation for crack initiation and propagation.

(3) Based on dislocation density and theoretical calculations, the major creep mechanisms for both alloys at 650 °C and 1000 MPa are identified as dislocation shearing and bypassing precipitates. Combining TEM analyses and theoretical calculations, it was found that at 700 °C and 700 MPa, the main creep mechanism for the U-0.043 alloy is micro-twinning and dislocation bypassing, while for the R-0.064 alloy, it involves extended stacking fault shearing of precipitates, dislocation bypassing and dislocation climb. At 750 °C and 460 MPa, dislocation bypassing and dislocation climbing are the predominant creep mechanisms for both alloys.

CRediT authorship contribution statement

Li-ming TAN: Conceptualization, Investigation, Data curation, Writing − Original draft; **Lin YE:** Formal analysis, Investigation, Data curation; **Heng DONG:** Formal analysis, Data curation; **Xiao-qiong OUYANG:** Investigation, Data curation; **Xiang-you XIAO:** Conceptualization, Methodology; **Qi ZENG:** Validation, **Jing-wei CHEN:** Funding acquisition; **Lan HUANG**: Conceptualization, Methodology, Validation, Writing − Review & editing, Supervision, Funding acquisition; **Feng LIU:** Conceptualization, Methodology, Validation, Writing − Review & editing, Supervision.

Declaration of competing interest

The authors declare that they have no known competing financial interests or personal relationships that could have appeared to influence the work reported in this paper.

Acknowledgments

This work was supported by the Natural Science Foundation of China (No. 52074366), the Top Ten Science and Technology Projects in Hunan Province, China (No. 2024GK1080), the Aero Engine Corporation of China (No. HFZL2022CXY029), the Young Elite Scientists Sponsorship Program by CAST, China (No. 2022QNRC001), the Natural Science Foundation of Hunan Province, China (No. 2021JJ40757), the Science and Technology Innovation Program of Hunan Province, China (No. 2021RC3131), the High Performance Computing Center of Central South University, and the Project supported by State Key Laboratory of Powder Metallurgy, Central South University, China.

References

[1] POLLOCK T M, TIN S. Nickel-based superalloys for advanced turbine engines: chemistry, microstructure and properties [J]. Journal of Propulsion and Power, 2006, 22(2): 361−374.

[2] YAO Zhi-hao, HOU Jie, CHEN Yang, XU Wen-yong, JIANG He, DONG Jian-xin. Effect of micron-sized particles on the crack growth behavior of a Ni-based powder metallurgy superalloy [J]. Materials Science and Engineering: A, 2022, 860: 144242.

[3] HARDY M C, ZIRBEL B, SHEN G, SHENKAR R. Developing damage tolerance and creep resistance in a high strength nickel alloy for disc applications [C]//Superalloys 2024. Warrendale: TMS, 2004: 83−90.

[4] TAN Li-ming, LI Yun-ping, DENG Wen-kai, LIU Yong, LIU Feng, NIE Yan, JIANG Liang. Tensile properties of three newly developed Ni-base powder metallurgy superalloys [J]. Journal of Alloys and Compounds, 2019, 804: 322−330.

[5] LIU Feng, WANG Ze-xin, TAN Li-ming, XIAO Xiang-you, LI Yun-ping, LI Xia, ZHANG Hua, ZHU Li-long, JIANG Liang, LIU Yong. Creep behaviors of fine-grained Ni-base powder metallurgy superalloys at elevated temperatures [J]. Journal of Alloys and Compounds, 2021, 867: 158865.

[6] TIAN Tian, HAO Zhi-bo, GE Chang-chun, LI Xing-gang, PENG Shi-qing, JIA Chong-lin. Effects of stress and temperature on creep behavior of a new third-generation powder metallurgy superalloy FGH100L [J]. Materials Science and Engineering: A, 2020, 776: 139007.

[7] ZHANG H P, BAI J M, LI X Y, LI X K, JIA J, LIU J T, ZHANG Y W. Segregation of alloying elements at planar faults during creep in the PM Ni-based superalloy FGH4096 [J]. Materials Letters, 2023, 349: 134741.

[8] TERZI S, COUTURIER R, GUÉTAZ L, VIGUIER B. Modelling the plastic deformation during high-temperature creep of a powder-metallurgy coarse-grained superalloy [J]. Materials Science and Engineering: A, 2008, 483/484: 598−601.

[9] BAI J M, ZHANG H P, LI X Y, LIU J T, SUN Q S, LIU C S, ZHANG Y W. Evolution of creep rupture mechanism in advanced powder metallurgy superalloys with tantalum addition [J]. Journal of Alloys and Compounds, 2022, 925: 166713.

[10] KIM Y K, KIM D, KIM H K, YOON E Y, LEE Y, OH C S, LEE B J. A numerical model to predict mechanical properties of Ni-base disk superalloys [J]. International Journal of Plasticity, 2018, 110: 123−144.

[11] LIU Feng, WANG Ze-xin, WANG Zi, ZHONG Jing, ZHAO Lei, JIANG Liang, ZHOU Run-hua, LIU Yong, HUANG Lan, TAN Li-ming, TIAN Yu-jia, ZHENG Han, FANG Qi-hong, ZHANG Li-jun, ZHANG Li-na, WU Hong, BAI Li-chun, ZHOU Kun. High-throughput method–accelerated design of Ni-based superalloys [J]. Advanced Functional Materials, 2022, 32(28): 2109367.

[12] KANG D S, KOIZUMI Y, YAMANAKA K, AOYAGI K, BIAN H, CHIBA A. Significant impact of yttrium microaddition on high temperature tensile properties of Inconel 713C superalloy [J]. Materials Letters, 2018, 227: 40−43.

[13] BIAN Wei-dong, ZHANG Hua-rui, ZHANG Xiao-li, GAO Ming, LI Jin-peng, LI Qing-ling, CUI Yong-shuang, ZHANG Hu. Comprehensive influence of Y on K417 superalloy: Purification, interactions among the alloy elements and high temperature properties [J]. Materials Science and Engineering: A, 2019, 755: 190−200.

[14] GUIMARÃES A V, da SILVEIRA R M S, de ALMEIDA L H D, ARAUJO L S, FARINA A B, FRANÇOIS-DILLE J A. Influence of yttrium addition on the microstructural evolution and mechanical properties of superalloy 718 [J]. Materials Science and Engineering: A, 2020, 776: 139023.

[15] BANOTH S, PALLEDA T N, SHIMAZU S, KAKEHI K. Yttrium's effect on the hot cracking and creep properties of a Ni-based superalloy built up by additive manufacturing [J]. Materials (Basel), 2021, 14(5): 1143−58.

[16] CAO Shu-ting, YANG Ya-qian, CHEN Bo, LIU Kui, MA Ying-che, DING Lei-lei, SHI Jun-jie. Influence of yttrium on purification and carbide precipitation of superalloy K4169 [J]. Journal of Materials Science & Technology, 2021, 86: 260−270.

[17] SONG Xiu, WANG Lei, LIU Yang, MA Hui-ping. Study on the mechanical performance of a Ni-based superalloy with trace rare earth element La additions [J]. Advanced Materials Research, 2012, 509: 177−181.

[18] LUIS E G A, BEDOLLA-JACUINDE A, GUERRA F V, RUIZ A. Influence of rare earth additions to an Inconel 718 alloy [J]. MRS Advances, 2020, 5(59): 3035−3043.

[19] SONG Xiu, WANG Lei, LIU Yang, MA Hui-ping. Precipitation characteristics and La effects on precipitates of a new 22Cr−14W−2Mo superalloy [J]. Rare Metals, 2010, 29(2): 132−137.

[20] CUI Chuan-yong, HAN Guo-ming, SUN Xiao-feng. Effect of Ce addition on the microstructures and mechanical properties of a Ni−Co-based superalloy [J]. Advanced Materials Research, 2011, 415/416/417: 2062−2065.

[21] LIU Long-fei, WU Shu-sen, CHEN Yang, LÜ Shu-lin. Oxidation behavior of RE-modified nickel-based superalloy between 950 °C and 1150 °C in air [J]. Transactions of Nonferrous Metals Society of China, 2016, 26(4): 1163−1169.

[22] REHMAN K, SHENG N, SANG Zhi-ru, XUN Shu-ling, WANG Zhen-jiang, XIE Jun, HOU Gui-chen, ZHOU Yi-zhou, SUN Xiao-feng. Comparative study of the reactive elements effects on oxidation behavior of a Ni-based superalloy [J]. Vacuum, 2021, 191: 110382.

[23] DENG Rui, LIU Feng, TAN Li-ming, ZHANG Si-yu, LIU Yong, HUANG Lan. Effects of scandium on microstructure and mechanical properties of RR1000 [J]. Journal of Alloys and Compounds, 2019, 785: 634−641.

[24] YE Lin, LIU Feng, DONG Heng, OUYANG Xiao-qiong, XIAO Xiang-you, TAN Li-ming, HUANG Lan. Investigation on the microstructure and mechanical properties of Ni-based superalloy with scandium [J]. Metals, 2023, 13(3): 611.

[25] TIAN Cheng-gang, HAN Guo-ming, CUI Chuan-yong, SUN Xiao-feng. Effects of stacking fault energy on the creep behaviors of Ni-base superalloy [J]. Materials & Design, 2014, 64: 316−323.

[26] YUAN Y, GU Y F, CUI C Y, OSADA T, TETSUI T, YOKOKAWA T, HARADA H. Creep mechanisms of U720Li disc superalloy at intermediate temperature [J]. Materials Science and Engineering: A, 2011, 528(15): 5106−5111.

[27] KOLBE M. The high temperature decrease of the critical resolved shear stress in nickel-base superalloys [J]. Materials Science and Engineering: A, 2001, 319/320/321: 383−387.

[28] SMITH T M, UNOCIC R R, DEUTCHMAN H, MILLS M J. Creep deformation mechanism mapping in nickel base disk superalloys [J]. Materials at High Temperatures, 2016, 33(4/5): 372−383.

[29] REPPICH B. Some new aspects concerning particle hardening mechanisms in γ' precipitating Ni-base alloys: I. Theoretical concept [J]. Acta Metallurgica, 1982, 30(1): 87−94.

[30] KIM Y K, KIM D, KIM H K, OH C S, LEE B J. An intermediate temperature creep model for Ni-based superalloys [J]. International Journal of Plasticity, 2016, 79: 153−175.

[31] ZHANG P, YUAN Y, SHEN S C, LI B, ZHU R H, YANG G X, SONG X L. Tensile deformation mechanisms at various temperatures in a new directionally solidified Ni-base superalloy [J]. Journal of Alloys and Compounds, 2017, 694: 502−509.

[32] CARON P, KHAN T, VEYSSIERE P. On precipitate shearing by superlattice stacking faults in superalloys [J]. Philosophical Magazine: Part A, 1988, 57(6): 859−875.

[33] KNOWLES D M, CHEN Q Z. Superlattice stacking fault formation and twinning during creep in γ/γ' single crystal superalloy CMSX-4 [J]. Materials Science and Engineering: A, 2003, 340(1/2): 88−102.

[34] VEYSSIERE P, DOUIN J, BEAUCHAMP P. On the presence of super lattice intrinsic stacking faults in plastically deformed Ni_3Al [J]. Materials Science and Engineering: A, 1985, 51(3): 469−483.

[35] CRUDDEN D J, MOTTURA A, WARNKEN N, RAEISINIA B, REED R C. Modelling of the influence of alloy composition on flow stress in high-strength nickel-based superalloys [J]. Acta Materialia, 2014, 75: 356−370.

含微量元素钪的粉末镍基高温合金的蠕变行为

谭黎明[1,2]，叶 林[1,2]，董 珩[1,2]，欧阳孝琼[1,2]，
肖祥友[1,2]，曾 琦[3]，陈竞玮[3]，黄 岚[1,2]，刘 锋[1,2]

1. 中南大学 粉末冶金国家重点实验室，长沙 410083；
2. 中南大学 粉末冶金研究院，长沙 410083；
3. 中国航发 湖南动力机械研究所，株洲 412000

摘 要：系统研究了两种含微量元素钪的粉末高温合金U720Li和RR1000的蠕变行为。结果表明，相比含0.043% Sc (质量分数)的U720Li合金(U-0.043)，含0.064% Sc (质量分数)的RR1000合金(R-0.064)在650 ℃和1000 MPa条件下具有更优异的蠕变性能，且在该条件下两种合金的主要蠕变机制均为位错剪切和绕过沉淀相。在 700 ℃和700 MPa条件下，U-0.043合金的主要蠕变机制为微孪晶和位错绕过，而在R-0.064合金中发现了堆垛层错切割γ'相、位错绕过和攀移现象。在750 ℃和460 MPa条件下，两种合金的主要变形机制均为位错绕过和位错攀移。

关键词：蠕变抗力；镍基高温合金；钪；粉末冶金；γ'析出相

(Edited by Wei-ping CHEN)